Pure Appl. Chem., Vol. 74, No. 10, pp. 1885–1894, 2002.
© 2002 IUPAC

Cation order/disorder in lithium transition-metal oxides as insertion electrodes for lithium-ion batteries*

E. Zhecheva[1,‡], R. Stoyanova[1], R. Alcántara[2], P. Lavela[2], and J.-L.Tirado[2]

[1]Institute of General and Inorganic Chemistry, Bulgarian Academy of Sciences, 1113 Sofia, Bulgaria; [2]Laboratorio de Química Inorgánica, Edificio C3, Primera Planta, Campus de Rabanales, Facultad de Ciencias, Universidad de Córdoba, 14071 Córdoba, Spain

Abstract: Results on the local cation ordering in layered lithium-nickel/cobalt oxides and metal-substituted lithium-manganese spinels are presented. It is shown that electron spin resonance of Ni^{3+} and Mn^{4+} and magnetic susceptibility measurements are powerful tools to monitor the short-range cation ordering in these compounds, which is not accessible by diffraction techniques. Thus, owing to the different strength of the 90° and 180° Ni^{3+}–O–$Ni^{3+/2+}$ exchange interactions, the distribution of Ni^{3+}/Ni^{2+} between the lithium and nickel layers in $Li_{1-x}Ni_{1+x}O_2$ with $0 < x < 0.4$ can be determined. For layered $LiNi_{1-y}Co_yO_2$ and spinel $LiMn_{2-x}Co_xO_4$ solid solutions, analysis of the temperature-independent EPR line width in terms of dipole–dipole and exchange interactions has been used to examine the local Ni^{3+}/Co^{3+} and Mn^{4+}/Co^{3+} ordering. The results obtained are correlated with the electrochemical intercalation of lithium in these compounds.

INTRODUCTION

Lithium intercalation compounds and reactions have attracted the interest of battery researchers since the early 1970s, owing to the increased energy density and higher operating voltage of a lithium cell as compared to the conventional rechargeable batteries. Substantial improvement in the performance of lithium rechargeable batteries was achieved by the application of the "rocking chair" or "lithium-ion" concept [1,2]. In 1990, Sony introduced the first commercial lithium rechargeable battery, in which layered $LiCoO_2$ and carbon were the active cathode and anode materials, respectively [3]. A vast number of transition-metal compounds with different lattice dimensionality have been studied as possible cathode materials for lithium-ion batteries [4,5]. However, practical interest is restricted to the following two groups of solids: $LiMO_2$ (M = Co, Ni) with a layer structure and $LiMn_2O_4$ with a spinel structure. At present, $LiCoO_2$ is still the prevalent positive electrode material for lithium-ion batteries, in spite of its relatively high cost and toxicity. The drawback of practical application of $LiNiO_2$ and $LiMn_2O_4$ results from the more exacting synthesis procedure and intercalation chemistry of these compounds [6,7]. Nevertheless, research efforts remain focused on the improvement of capacity and cycleability of lithium-nickel and lithium-manganese oxides by changing the preparation procedure (precursor, temperature of preparation [5,8]) and composition (metal doping [4–6,9]). In this paper, data concerning

*Lecture presented at the 10th International Symposium on Solubility Phenomena, Varna, Bulgaria, 22–26 July 2002. Other lectures are published in this issue, pp. 1785–1920.

‡Corresponding author: E-mail: zhecheva@svr.igic.bas.bg

the effect of the synthesis conditions on the local cation distribution in LiNi/CoO_2 and $LiMn_{2-x}M_xO_4$ (M = Co, Mg) are presented. Since magnetic properties are sensitive to the cation distribution, magnetic measurements (electron spin resonance and magnetic susceptibility measurements) were used to monitor the short-range cation ordering in these compounds, which is not possible by means of diffraction techniques.

RESULTS

Layered LiNi/CoO_2 oxides

$Li_{1-x}Ni_{1+x}O_2$

Layered $LiNiO_2$ is isostructural to $LiCoO_2$, which has a trigonal crystal structure (Fig. 1): the alternating ordering of Li^+ and Co^{3+}/Ni^{3+} in the octahedral sites (denoted as *3a* and *3b*) of the (111) planes in the close oxygen packing results in discrete LiO_2 and Co/NiO_2 layers (*R-3m* space group) [10,11]. The two-dimensional motion of the Li^+ ions between the strongly bonded Co/NiO_2 layers provides a high ion conductivity. However, contrary to $LiCoO_2$, solid solutions of the type $Li_{1-x}Ni_{1+x}O_2$ are formed in the Li–Ni–O system. Due to the difficult oxidation of Ni^{2+} to Ni^{3+} and the volatility of the lithium compounds, nonstoichiometric oxides with $0.005 < x < 0.2$ are usually obtained [12–14]. Preparing compositions with $x \rightarrow 0$ is very difficult, and an "ideal" stoichiometric $LiNiO_2$ has not yet been achieved [12–14]. The presence of nonstoichiometric Ni^{2+} ions in lithium-rich layers frustrates the long-range Li–Ni ordering, culminating at a critical lithium concentration of $x = 0.38$ in a random distribution of Li^+, Ni^{3+}, and Ni^{2+} ions within the cubic crystal structure (NaCl type) [10]. On the other hand, the occupancy of the "impurity" Ni^{2+} ions in the Li-site of nonstoichiometric $Li_{1-x}Ni_{1+x}O_2$ compositions hinders lithium transport.

Based on the sensitivity of the magnetic properties of $Li_{1+x}Ni_{1-x}O_2$ to its stoichiometry, we have applied electron paramagnetic resonance (EPR) spectroscopy of low-spin Ni^{3+} to the determination of the amount of Ni^{3+}/Ni^{2+} ions in both lithium and nickel layers in $Li_{1-x}Ni_{1+x}O_2$ with $0 < x < 0.4$. The EPR spectrum of Ni^{3+} (S = 1/2 with a ^2E_g ground term) in $Li_{1-x}Ni_{1+x}O_2$ is an exchange-narrowed Lorentzian with g = 2.137. The temperature variation in the EPR spectrum of Ni^{3+} is a result of the development of weak ferromagnetic intralayer and strong antiferromagnetic interlayer Ni^{3+}–O–Ni^{2+} exchange interactions (90° and 180° configuration, respectively) [15]. Above the magnetic correlation temperature (>210 K), the line width shows broadening due to the phonon modulation of the anisotropic spin–spin interactions: $\Delta H_{pp} = \Delta H_{pp}^{o} + bT$. The $d\Delta H_{pp}/dT$ coefficient is proportional to the isotropic exchange integral, to the coordination number of exchange-coupled particles, and to the distance between them. Figure 2 presents the dependence of the $d\Delta H_{pp}/dT$ coefficient on the stoichiometry in

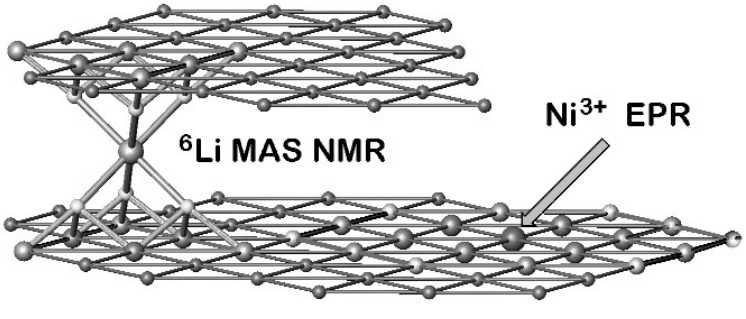

Fig. 1 Schematic representation of the layered structure of LiNi/CoO_2. The metal clusters determined by Ni^{3+} EPR and ^6Li (^7Li) MAS NMR are denoted. For simplicity, the oxygen atoms are omitted except for the NMR-cluster.

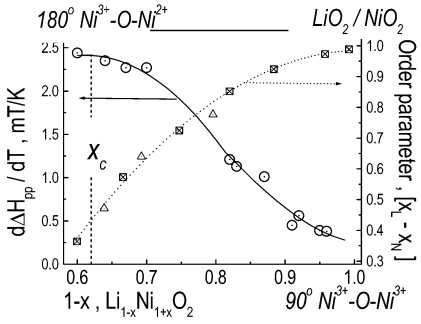

Fig. 2 The $d\Delta H_{pp}/dT$ coefficient and order parameter vs. lithium content in $Li_{1-x}Ni_{1+x}O_2$. The data for the order parameter are taken from refs. [4,5].

$Li_{1-x}Ni_{1+x}O_2$ compositions. Two regions can be distinguished: one for $0.6 \leq (1 - x) \leq 0.7$, where $d\Delta H_{pp}/dT$ has a poor dependence on $(1 - x)$, and another for $0.7 < (1 - x) < 1$, where $d\Delta H_{pp}/dT$ sharply decreases as $(1 - x)$ increases. The observed dependence reveals the corresponding changes in the composition of the Ni^{3+}–O–$Ni^{3+/2+}$ shell as the Li amount increases from 0.6 to 1. For $0.6 \leq (1 - x) \leq 0.7$, where Li^+, Ni^{2+}, and Ni^{3+} are nearly equal in amount, the poor dependence of $d\Delta H_{pp}/dT$ on $(1 - x)$ reveals Ni^{3+}– and Ni^{2+}– segregation into two adjacent planes. At $(1 - x) > 0.7$, where the Ni^{2+} amount decreases, the reduction of the $d\Delta H_{pp}/dT$-value with $(1 - x)$ indicates restriction in the Ni^{3+}–O–Ni^{2+} interactions due to restriction of the Ni^{2+}-segregation. In the same concentration range, long-range Li–Ni ordering takes place. As a measure of the long-range Li–Ni ordering in $Li_{1-x}Ni_{1+x}O_2$ solid solutions, Dahn et al. have introduced an order parameter, which gives the difference in the lithium occupancy in the two distinct crystallographic sites (Fig. 2) [10]. Using data for the lithium occupancy in $Li_{1-x}Ni_{1+x}O_2$, from the value of the $d\Delta H_{pp}/dT$ coefficient we can estimate the Ni^{2+}/Ni^{3+} distribution into the lithium- and nickel-rich layer: $d\Delta H_{pp}/dT = 3[(Ni^{2+}{}_{LiO2})\cdot(Ni^{3+}{}_{NiO2}) + (Ni^{2+}{}_{NiO2})\cdot(Ni^{3+}{}_{LiO2})]b_c$, where b_c is the $d\Delta H_{pp}/dT$-coefficient for the samples with $0.6 \leq (1 - x) \leq 0.7$. Based on this analysis, it seems that for the samples with a small lithium deficiency ($x < 0.1$) nonstoichiometric Ni^{2+} reside in both layers with an almost equal amount: $(Li_{1-x}Ni_x{}^{2+})_{3a}(Ni^{3+}{}_{1-x}Ni^{2+}{}_x)_{3b}$. The appearance of "extra" Ni^{2+} ions in the LiO_2-layer has been shown to impair the electrochemical performance of nonstoichiometric $Li_{1-x}Ni_{1+x}O_2$ when used as cathode materials in lithium-ion batteries [12,16].

For nearly stoichiometric $Li_{1-x}Ni_{1+x}O_2$ ($0 < x < 0.05$), the competition between the two-dimensional ferromagnetic Ni^{3+}–O–Ni^{3+} interactions with a 90°-configuration in the NiO_2-layers and the Jahn–Teller effect for Ni^{3+} ions cause a complex temperature behavior of the EPR line width between 10 and 400 K [15,17–19]. For samples with the same lithium content, but prepared at different temperatures, there is a clear dependence of the value of the $d\Delta H_{pp}/dT$ coefficient on the synthesis temperature [20]. By extrapolation of x to 0, one obtains $d\Delta H_{pp}/dT = 0.26$ and $0.42\ mT\cdot K^{-1}$ for the "ideal" stoichiometric $LiNiO_2$ prepared at 700 and 800 °C, respectively. This dependence can be explained by a model that accounts for the contribution of Ni^{3+} and Li^+ ions from LiO_2- and NiO_2-layers to the 90° Ni^{3+}–O^{2-}–Ni^{3+} interactions. Based on this analysis, it seems that cation mixing between the layers takes place, which is more significant for the sample prepared at a higher temperature. The reaction of cation mixing will display the same effect on the electrochemical properties of $LiNiO_2$, as in the case of lithium nonstoichiometry. In fact, $LiNiO_2$ compositions used as cathode materials in lithium-ion batteries are usually obtained at 700 °C [14].

$LiNi_{1-y}Co_yO_2$

The $Li_{1-x}(Ni_{1-y}Co_y)_{1+x}O_2$ solid solutions have electrochemical properties better than those of $Li_{1-x}Ni_{1+x}O_2$ and $LiCoO_2$. It is established that small cobalt additives to $Li_{1-x}Ni_{1+x}O_2$ stabilize both the Ni^{3+} ions and the layered crystal structure [21,22]. With increasing cobalt content, the trigonal distor-

tion of the crystal lattice increases and the deviation from the stoichiometry of $Li_{1-x}(Ni_{1-y}Co_y)_{1+x}O_2$ decreases. From magnetic susceptibility measurements, it follows that the lithium nonstoichiometry is associated with Ni^{2+} ions only. Structural data on $LiNi_{1-y}Co_yO_2$ with stoichiometric compositions show that the crystallographic parameters vary almost linearly between those of the end members $LiNiO_2$ and $LiCoO_2$ (Vegard's-like behavior [22]).

Due to their electronic configuration (d^6 low-spin), Co^{3+} ions act as "magnetic dilutants" of the magnetically coupled Ni^{3+} ions in $LiN_{1-y}Co_yO_2$ solid solutions. In this case, analysis of the temperature-independent EPR line width, $\Delta H_{pp}{}^{o}$, in terms of dipole–dipole and exchange interactions, has been used to examine the local Ni/Co distribution in $LiN_{1-y}Co_yO_2$, which is not possible by means of X-ray diffraction (XRD) [23]. With increasing amount of the diamagnetic Co^3 ions in stoichiometric $LiN_{1-y}Co_yO_2$, the EPR line width increases, passes through maximum at $y = 0.38$, and then decreases. This behavior of the EPR line width is a consequence of the simultaneous development of magnetic dipole–dipole and exchange interactions.

With sample compositions for which $0 < y < 0.38$, the line broadening reveals dilution of the intralayer ferromagnetic Ni^{3+}–O–Ni^{3+} interactions by diamagnetic Co^{3+} ions, as well as suppression of the magnetic dipole–dipole interactions:

$$\Delta H_{pp} = \text{const}\cdot g^2\cdot S\,(S+1)\sum(1/r_{ik}{}^6)/\{[8/3S(S+1)z]^{1/2}\cdot J\}, \quad (1)$$

where z is the number of paramagnetic ions around Ni^{3+} in the NiO_2-layers, and J is the exchange integral between the Ni^{3+} ions. At $y \approx 0.38$, where the EPR line width reaches its maximum, the effect of the exchange interactions on the EPR line width terminates. Having in mind that exchange interactions are developed in an infinite cluster of bonds, the appearance of the exchange interactions in $LiN_{1-y}Co_yO_2$ at $y \approx 0.38$ corresponds to the percolation threshold for Ni^{3+}–Ni^{3+} bonds in these solid solutions. However, for a triangular lattice, the percolation threshold of bonds is 0.5, which indicates that the Co^{3+}–Co^{3+} interatomic interactions are higher than the Ni^{3+}–Ni^{3+} interactions.

Magnetic dipolar interactions explain the line width changes observed for the samples with high cobalt content ($y > 0.4$). According to the method of moments, the contribution of the dipole–dipole interactions to the EPR line width is expressed by:

$$\Delta H_{pp}{}^2 = \text{const}\cdot g^2\cdot S\,(S+1)\sum(1/r_{ik}{}^6) \quad (2)$$

For the triangular lattice of Ni^{3+}/Co^{3+} in $LiN_{1-y}Co_yO_2$, calculations show that the effect of the Ni^{3+} ions on the magnetic dipolar broadening of the EPR line width is negligible at a distance larger than $2a$ (smaller than 10 mT). For simplicity, we shall denote the ions located at a distance $r > 2a$ and $r \leq 2a$ as isolated and nonisolated Ni^{3+}, respectively.

Applying analysis of the EPR line width, we can extract information on the Ni^{3+} distribution in $LiN_{1-y}Co_yO_2$ solid solutions obtained at different temperatures [23]. The EPR spectra of cobalt-rich $LiN_{1-y}Co_yO_2$ with $y = 0.9$ prepared at low temperatures contain two signals with different line widths and slightly differing g-values ($g = 2.137$ and 2.142 for the broader and the narrower signal, respectively, Fig. 3). These two signals correspond to two kinds of low-spin Ni^{3+} characterized by different Ni^{3+}–O^{2-} bond covalencies and metal ion surroundings. An EPR signal with $g = 2.142$ was found for Ni^{3+}-doped $LiCoO_2$ [24]. Having in mind the parameters of the two EPR signals in $LiN_{1-y}Co_yO_2$, we can assign them to nonisolated and isolated Ni^{3+} ions (the broader and narrower signals), respectively.

The Ni/Co distribution displays a strong dependence on the preparation conditions (Fig. 4). When the preparation temperature increases, the content of nonisolated Ni^{3+} also increases, whereas the content of isolated Ni^{3+} decreases. In a case of random Ni/Co distribution, the probability for a given Ni^{3+} ion to have only diamagnetic Co^{3+} neighbors at a distance $2a$ (totally 18 neighbors) can be calculated as: $P_o = (^{18}{}_0)y^{18-0}(1-y)^0$, where $(^{18}{}_0)$ is the binomial coefficient and $(1 - y)$ and y corresponds to the nickel and cobalt content, respectively. For the sample with 0.13 nickel content, the probability for the appearance of isolated Ni^{3+} ions (a $NiCo_{18}$ cluster) is 0.08. If this value is compared with those obtained from EPR (Fig. 4), the deviations in the amount of isolated Ni^{3+} from the calculated values show unam-

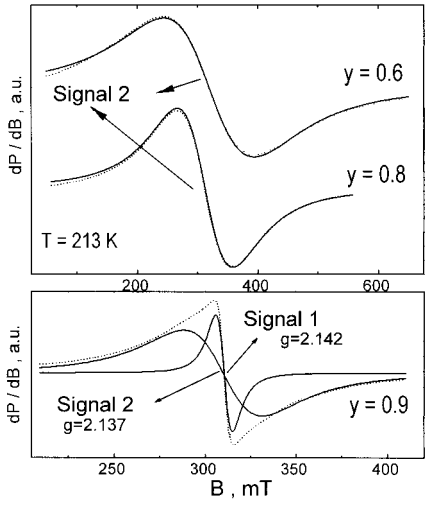

Fig. 3 EPR spectra of Ni^{3+} in $LiNi_{1-y}Co_yO_2$ compositions obtained at 650 °C.

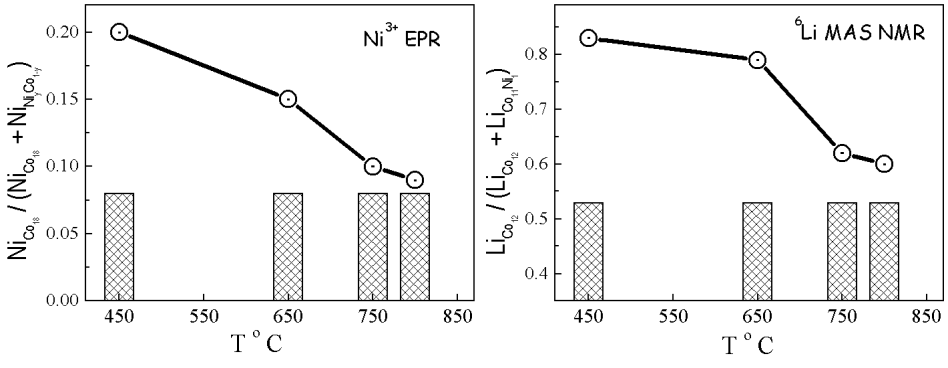

Fig. 4 Amount of isolated Ni^{3+} ions determined from EPR and intensity ratio between the signal at 0 ppm and the signal at –15 ppm determined from ^{6}Li MAS NMR vs. the preparation temperature of $LiNi_{0.13}Co_{0.87}O_2$. The corresponding values for statistical Ni/Co distribution are presented.

biguously a nonrandom Ni/Co distribution in the Ni/CoO_2 layers for the low-temperature samples, (i.e., it is a case of compositional inhomogeneities at a microscopic scale). With increasing preparation temperature, the amount of isolated Ni^{3+} tends to be a lower value corresponding to the random distribution.

Varieties of the local Ni/Co distribution in $LiN_{0.13}Co_{0.87}O_2$ obtained at different temperatures are also observed with ^{6}Li high-speed magic-angle spinning (MAS) NMR of these samples. The room-temperature spectra for cobalt-rich compositions consist of a set of sharp lines in the –200 to 200 ppm regions and the corresponding side-bands [23]. The intense line at ca. 0 ppm was the only signal observed in the spectra of pure $LiCoO_2$. Thus, it can be ascribed to lithium ions surrounded by Co^{3+} ions only [25]: $3Co^{3+}$ in the upper and $3Co^{3+}$ in the lower plane, that is, $(Li)(Co_3Co_3)^I(Co_3Co_3)^{II}$ configuration (the symbols ^{I} and ^{II} are related to first and second metal surrounding of Li, respectively, Fig. 1). Besides, other lines at –15, –30…. ppm have to be ascribed to the presence of one, two, or more Ni^{3+} as second metal neighbors [25]: $(Li)(Co_3Co_3)^I(Ni_zCo_{6-z})^{II}$ with z = 1, 2,… respectively. The changes in ratio between the peak at 0 ppm and the negatively shifted peak at –15 ppm

reveal that a significant Ni/Co redistribution takes place between 650 and 750 °C (Fig. 4). Using the binominal probability for a random Co/Ni distribution, the ratio of $(Li)(Co_3Co_3)^{I}(Co_3Co_3)^{II}$ and $(Li)(Co_3Co_3)^{I}(Ni_1Co_5)^{II}$ configurations is 0.53. Thus, a trend toward random Ni/Co distribution with increasing preparation temperature of $LiNi_{1-y}Co_yO_2$ solid solutions is also observed in the ^6Li NMR spectra. At first glance, it seems that there is a good correlation between the result obtained by ^6Li MAS NMR and Ni^{3+} EPR, but close inspection shows that ^6Li MAS NMR gives evidence of a small-scale Ni/Ni and Co/Co segregation even for the high-temperature $LiNi_{0.13}Co_{0.87}O_2$ (Fig. 4).

Accordingly, there are strong changes in the profiles of the electrochemical lithium deintercalation/intercalation curves of $LiNi_{0.13}Co_{0.87}O_2$ compositions when the preparation temperature increases from 650 to 800 °C (Fig. 5). In fact, Co-rich $LiNi_{1-y}Co_yO_2$ compositions used as cathode materials in lithium-ion batteries are usually obtained at temperatures higher than 750 °C.

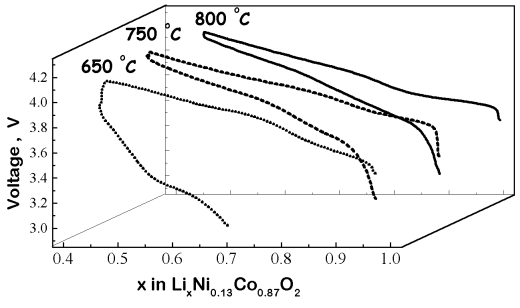

Fig. 5 Results of the step potential electrochemical spectroscopy of $LiNi_{0.13}Co_{0.87}O_2$ obtained at different temperatures.

Spinel $LiMn_{2-x}M_xO_4$ oxides

The $LiMn_2O_4$ spinel oxide has a 3-dimensional structure in which the Li^+ and the $Mn^{4+/3+}$ ions occupy the *8a* tetrahedral and *16d* octahedral sites of the cubic close oxygen packing, respectively. A strongly bonded edge-shared octahedral $[Mn_2]O_4$ array permits a reversible extraction of the Li^+ ions without collapse of the spinel framework. In order to improve the cycling stability of lithium-manganese spinels, doping with transition and nontransition metal ions has been successfully applied. The role of metal dopants is to stabilize the spinel structure during the lithium cycling, to limit the depth of lithium intercalation/ deintercalation, and to increase the potential where Li electrochemical reaction takes place [4,26–28]. Irrespective of the fact that there are many data concerning the effect of metal doping on the electrochemical properties of $LiMn_2O_4$, less attention has been paid to the effect of the thermal history on the cationic distribution in spinel-substituted compositions. Here, we provide data concerning the cation distribution in Co and Mg-substituted $LiMn_2O_4$ spinels, as well as its effect on the electrochemical performance.

$LiMn_{2-x}Co_xO_4$

In $LiMn_{2-x}Co_xO_4$, Co^{3+} substitutes isomorphically for the Jahn–Teller Mn^{3+} ions. When prepared at 750 °C and slowly cooled to room temperature, $LiMnCoO_4$ is stoichiometric in respect to oxygen: $Li_{8a}[Mn^{4+}Co^{3+}]_{16d}O_4$. During heating, a small oxygen loss takes place at temperatures higher than 500 °C. Thermal dissociation into a Li-free spinel and a Li-rich oxide takes place above 800 °C. Correspondingly, the mean oxidation state of (Co + Mn) decreases, the temperature of sharp decrease being 800 °C (Fig. 6). In the monophase region, small differences are observed in the IR spectra of $LiMnCoO_4$: a weak fine structure is superimposed to the well-known spinel bands of the low-temperature phases. The fine structure fades away for the compositions quenched from high temperatures. This result implies that the Co/Mn distribution in $LiMnCoO_4$ is sensitive to the quenching temperature.

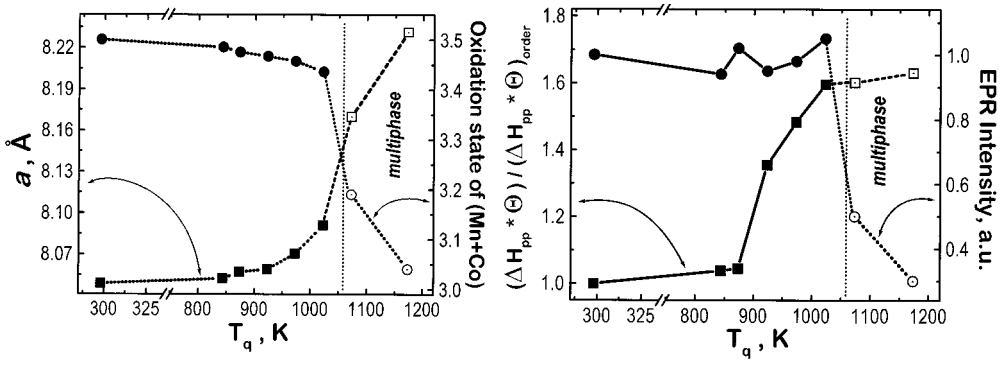

Fig. 6 Unit cell parameter, a, mean oxidation state of (Mn + Co), EPR signal intensity and normalized line width, $(\Delta H_{pp*}\Theta) / (\Delta H_{pp*}\Theta)_{\text{order}}$, for $LiMnCoO_4$ quenched from different temperatures.

EPR of Mn^{4+} in $LiMnCoO_4$ (S = 3/2 with a $^4A_{2g}$ ground term) offers evidence of a short-range Co/Mn ordering [29]. Since Co^{3+} is diamagnetic, the only paramagnetic species in $LiMnCoO_4$ is the Mn^{4+} ion. For a $LiMnCoO_4$ spinel cooled slowly in an O_2 atmosphere, the EPR spectrum consists of the single Lorentzian line with g = 2.002 coming from the antiferromagnetically coupled Mn^{4+} ions in the *16d* spinel sites. For samples quenched from temperatures between 550 and 750 °C, an additional broad EPR signal with $g > 2.2$ grows in intensity. The appearance of this broad signal can be related to the slight decrease in the mean oxidation state of (Co + Mn) observed in this temperature range. This can be understood if we suppose that there are extended defects accommodating Mn^{4+}/Mn^{3+}, which cause the appearance of the additional EPR signal. The same situation has been found for undoped $LiMn_2O_4$ [30], but the difference in the EPR parameters signifies incorporation of Co in these defects.

The other feature of the EPR spectrum of $LiMnCoO_4$ is associated with the line width, ΔH_{pp}, of the main signal coming from the exchange coupled Mn^{4+}. With increasing quenching temperature, the line width undergoes a significant broadening (Fig. 6). Even after thermal dissociation (above 800 °C), a weak EPR signal due to Mn^{4+} in $LiMnCoO_4$ is still observable for the multiphase system. The temperature variation of the signal intensity obeys the Curie–Weiss law. The Weiss constant, Θ, depends on the metal–metal distance, which, on the other hand, is sensitive to the quenching temperature. The observed difference in the EPR line width for the different $LiMnCoO_4$ samples permits differentiating between them with respect to the first metal shell of Mn^{4+}.

To estimate the number of paramagnetic and diamagnetic metal neighbors of Mn^{4+}, the EPR line width was analyzed in terms of magnetic dipole–dipole and exchange interactions. Expressing the exchange integral J in eq. 1 by the experimentally accessible Weiss constant, Θ, the relation between the EPR line width, ΔH_{pp}, and the number of paramagnetic neighbors, z, can be estimated:

$$z^{3/2} = (\Delta H_{pp}\cdot\Theta)\cdot r_{\text{M–M}}{}^6/g \tag{3}$$

Figure 6 gives the number of paramagnetic neighbors of Mn^{4+} (normalized vs. slow-cooled $LiMnCoO_4$, z_q/z_{slow}) for samples quenched from different temperatures. The results obtained indicate that the number of paramagnetic neighbors of Mn^{4+} increases with the increase in quenching temperature, the temperature of the sharp increase being 650 °C. Using an EPR "standard" (in our case, Li_2MnO_3 with well-documented crystal structure data), we have estimated the mean number of paramagnetic ions in the $LiMnCoO_4$ compositions. For the high-temperature samples, the mean number of paramagnetic neighbors of Mn^{4+} is nearly 3, which corresponds to that of the statistical distribution. However, for the spinel slowly cooled to room temperature, the mean number of Mn^{4+} paramagnetic neighbors tends to 2, which means a small-scale Mn^{3+}/Co^{3+} ordering. Two types of 1:1 cation ordering in *16d* spinel sites are known [31]. Both of them are similar with respect to the first metal shell: every ion's first neighbors are 4 "alien" and 2 "allied" ions, i.e., $4Co^{4+} + 2Mn^{2+}$ for every Mn^{4+}. Second and

third metal shells allow differentiating between the two types of 1:1 ordering. Since the first metal neighbors have the major contribution to the EPR line width (about 95 % in this case), the two types of cation ordering are not clearly distinguishable by EPR.

Thus, for spinels quenched from temperatures higher than 650 °C, the Co/Mn ions are statistically distributed in the octahedral spinel sites, while during slow cooling Co/Mn tends to order. Accordingly, low- and high-temperature $LiMn_{2-x}Co_xO_4$ display differences in their intercalation properties [32]. The use of these materials as the cathodic active compound in lithium cells reveals a higher capacity but a lower capacity retention in the 3–4 V regions for the sample quenched from 750 °C as compared with the slow-cooled composition (Fig. 7).

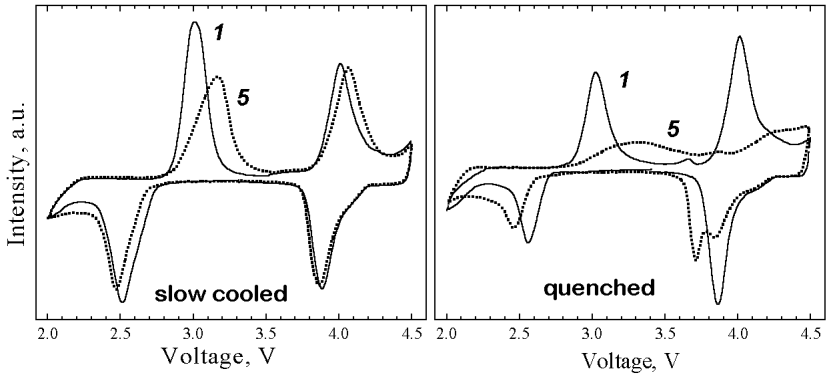

Fig. 7 Cell potential (V) versus current intensity (a.u.) obtained by SPES of slow-cooled (solid lines) and quenched (dotted lines) $LiMn_{1.4}Co_{0.6}O_4$ for the first and fifth cycles.

$LiMg_{0.5}Mn_{1.5}O_4$

The $Li_{8a}(Mg_{0.5}Mn^{4+}{}_{1.5})_{16d}O_4$ spinel is a well-known example of a spinel with an 1:3 cation ordering in *16d* sites [33,34]. Using the lactate precursor method, we succeeded preparing at 450 °C a $LiMg_{0.5}Mn_{1.5}O_4$ spinel with a statistical (according to XRD and IR) cation distribution in the *16d* spinel sites. Heating at 600 °C irreversibly transforms the disordered $LiMg_{0.5}Mn_{1.5}O_4$ spinel into an ordered one (Fig. 8). The EPR spectra of Mn^{4+} in ordered and disordered $LiMg_{0.5}Mn_{1.5}O_4$ consist of a Lorentzian line with $g = 2.002$ resulting from the ferromagnetically coupled Mn^{4+} ions. Similarly to the case of $LiMnCoO_4$, the EPR line width increases when a transition from ordered to disordered spinel proceeds (Fig. 8), and correlates well with the mean number of paramagnetic neighbors of Mn^{4+} in the two structural varieties (4 vs. 4.5 Mn^{4+}, respectively).

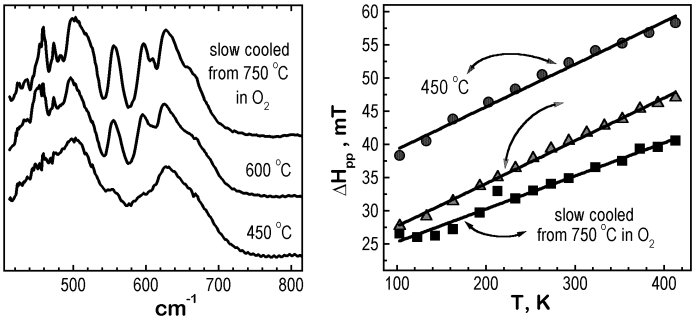

Fig. 8 IR spectra and temperature variation in the EPR line width (ΔH_{pp}) for $LiMg_{0.5}Mn_{1.5}O_4$ spinels obtained at different temperatures.

The use of $LiMg_{0.5}Mn_{1.5}O_4$ spinels as the cathodic active compound in 3-V lithium cells reveals that the disordered phase obtained at 450 °C has a reduced capacity as compared to the ordered spinel obtained at 600 °C. However, the lower capacity of the low-temperature sample may be also due to structural defects (such as exchange of Li and Mg atoms in their sites and/or the existence of traces of Mg atoms in octahedral empty sites together with traces of Mn^{3+}). This would impede the optimal occupancy of alkaline ion sites in the structure.

ACKNOWLEDGMENTS

The authors acknowledge financial support from EU (contracts JOU2-CT93-0326 and ERB CIPD CT94-0501), National Science fund of Bulgaria (Contract CH-810/1998), and CICYT (contract MAT99-0741).

REFERENCES

1. M. B. Armand. In *Materials for Advanced Batteries*, D. W. Murphy, J. Broadhead, B. C. H. Steele (Eds.), p. 145, Plenum, New York (1980).
2. B. Di Pietro, M. Patriarca, B. Scrosati. *J. Power Sources* **8**, 289 (1982).
3. T. Nagaura and K. Tazawa. *Prog. Battery Solar Cells* **9**, 20 (1990).
4. M. Winter, J. O. Besenhard, M. Spahr, P. Novák. *Adv. Mater.* **10**, 725 (1998).
5. R. Alcantara, P. Lavela, J. L. Tirado, E. Zhecheva, R. Stoyanova. *J. Solid State Electrochem.* **3**, 121 (1999).
6. C. Delmas, M. Ménétrier, L. Croguennec, S. Levasseur, J. P. Pérès, C. Pouillerie, G. Prado, L. Fournès, F. Weill. *Int. J. Inorg. Mater.* **1**, 11 (1999).
7. J. M. Tarascon, W. R. Mc Kinon, F. Coowar, T. N. Bowner, G. Amatucci, D. Guyomard. *J. Electrochem. Soc.* **141**, 1421 (1994).
8. J. P. Pereira-Ramos. *J. Power Sources* **54**, 120 (1995).
9. C. Delmas, M. Ménétrier, L. Croguennec, I. Saadoune, A. Rougier, C. Pouillerie, G. Prado, M. Grüne, L. Fournès. *Electrochim. Acta* **45**, 243 (1999).
10. W. Li, J. N. Reimers, J. R Dahn. *Phys. Rev. B* **46**, 3236 (1992).
11. I. J. Pickering, J. T. Lewandowski, A. J. Jacobson, J. A. Goldstone. *Solid State Ionics* **53–56**, 405 (1992).
12. A. Rougier, P. Gravereau, C. Delmas. *J. Electrochem. Soc.* **143**, 1168 (1996).
13. H. Arai, S. Okada, H. Ohtsuka, M. Ichimura, J. Yamaki. *Solid State Ionics* **80**, 261 (1995).
14. V. Bianchi, D. Caurant, N. Baffier, C. Belhomme, E. Chappel, G. Chouteau, S. Bach, J. P. Pereira-Ramos, A. Sulpice, P. Wilmann. *Solid State Ionics* **140**, 1 (2001).
15. R. Stoyanova, E. Zhecheva, C. Friebel. *Solid State Ionics* **73**, 1 (1994).
16. V. Bianchi, S. Bach, C. Belhomme, J. Farcy, J. P. Pereira-Ramos, D. Caurant, N. Baffier, P. Willman. *Electrochim. Acta* **46**, 999 (2001).
17. R. Stoyanova, E. Zhecheva, C. Friebel. *J. Phys. Chem. Solids* **54**, 9 (1993).
18. C. B. Azzoni, A. Paleari, V. Massaroti, M. Bini, D. Capsoni. *Phys. Rev. B* **53**, 703 (1996).
19. A.-L. Barra, G. Chouteau, A. Stepanov, A. Rougier, C. Delmas. *Eur. Phys. J. B* **7**, 551 (1999).
20. R. Alcantara, P. Lavela, J. L. Tirado, R. Stoyanova, E. Kuzmanova, E. Zhecheva. *Chem. Mater.* **9**, 2145 (1997).
21. C. Delmas and I. Saadoune. *Solid State Ionics* **53–56**, 370 (1992).
22. E. Zhecheva and R. Stoyanova. *Solid State Ionics* **66**, 143 (1993).
23. R. Stoyanova, E. Zhecheva, R. Alcantara, P. Lavela, J. L. Tirado. *Solid State Commun.* **102**, 457 (1997).
24. S. Angelov, C. Friebel, E. Zhecheva, R. Stoyanova. *J. Phys. Chem. Solids* **53**, 443 (1992).

25. C. Marichal, J. Hirshinger, P. Granger, M. Ménétrier, A. Rougier, C. Delmas. *Inorg. Chem.* **34**, 1773 (1995).
26. G. Pistoia, A. Antonini, R. Rosati, C. Bellito. *J. Electroanal. Chem.* **410**, 115 (1996).
27. H. Hosoya, H. Ikuta, M. Wakihara. *Solid State Ionics* **111**, 153 (1998).
28. H. Kawai, M. Nagata, H. Tukamoto, A. West. *J. Mater. Chem.* **8**, 837 (1998).
29. R. Stoyanova, E. Zhecheva, M. Gorova. *J. Mater. Chem.* **10**, 1377 (2000).
30. R. Stoyanova, M. Gorova, E. Zhecheva. *J. Phys. Chem. Solids* **61**, 609 (2000).
31. D. Gryffroy and R. E. Vandenberghe. *J. Phys. Chem. Solids* **53**, 777 (1992).
32. E. Zhecheva, R. Stoyanova, M. Gorova, P. Lavela, J. L. Tirado. *Solid State Ionics* **140**, 19 (2001).
33. G. Blasse. *Philips Res. Rep.* 1 (1964).
34. P. Strobel, A. Ibara Palos, M. Anne, F. Le Cras. *J. Mater. Chem.* **10**, 429 (2000).